BNL-221840-2021-JAAM

Probing charge density wave phases and the Mott transition in 1T-TaS2I by inelastic light scattering

S. D. Mijin, C. Petrovic

To be published in "PHYSICAL REVIEW B"

June 2021

Condensed Matter Physics and Materials Science Department

Brookhaven National Laboratory

U.S. Department of Energy

USDOE Office of Science (SC), Basic Energy Sciences (BES) (SC-22)

DISCLAIMER

Probing charge density wave phases and the Mott transition in $1T$-TaS_2 by inelastic light scattering

S. Djurdjić Mijin,[1] A. Baum,[2] J. Bekaert,[3] A. Šolajić,[1] J. Pešić,[1] Y. Liu,[4,*] Ge He,[2] M. V. Milošević,[3] C. Petrovic,[4] Z. V. Popović,[1,5] R. Hackl,[2] and N. Lazarević[1]

[1] *Center for Solid State Physics and New Materials, Institute of Physics Belgrade, University of Belgrade, Pregrevica 118, 11080 Belgrade, Serbia*
[2] *Walther Meissner Institut, Bayerische Akademie der Wissenschaften, 85748 Garching, Germany*
[3] *Department of Physics, University of Antwerp, Groenenborgerlaan 171, B-2020 Antwerp, Belgium*
[4] *Condensed Matter Physics and Materials Science Department, Brookhaven National Laboratory, Upton, NY 11973-5000, USA*
[5] *Serbian Academy of Sciences and Arts, Knez Mihailova 35, 11000 Belgrade, Serbia*

(Dated: June 14, 2021)

We present a polarization-resolved, high-resolution Raman scattering study of the three consecutive charge density wave (CDW) regimes in $1T$-TaS_2 single crystals, supported by *ab initio* calculations. Our analysis of the spectra within the low-temperature commensurate (C-CDW) regime shows $P\bar{3}$ symmetry of the system, thus excluding the previously proposed triclinic stacking of the "star-of-David" structure, and promoting trigonal or hexagonal stacking instead. The spectra of the high-temperature incommensurate (IC-CDW) phase directly project the phonon density of states due to the breaking of the translational invariance, supplemented by sizeable electron-phonon coupling. Between 200 and 352 K, our Raman spectra show contributions from both the IC-CDW and the C-CDW phase, indicating their coexistence in the so-called nearly-commensurate (NC-CDW) phase. The temperature-dependence of the symmetry-resolved Raman conductivity indicates the stepwise reduction of the density of states in the CDW phases, followed by a Mott transition within the C-CDW phase. We determine the size of the Mott gap to be $\Omega_{\rm gap} \approx 170 - 190$ meV, and track its temperature dependence.

I. INTRODUCTION

Quasi-two-dimensional transition metal dichalcogenides (TMDs), such as the various structures of $TaSe_2$ and TaS_2 have been in the focus of various scientific investigations over the last 30 years, mostly due to the plethora of charge density wave (CDW) phases [1, 2]. Among all TMD compounds $1T$-TaS_2 stands out because of its unique and rich electronic phase diagram [3–6]. It experiences phase transitions at relatively high temperatures, making it easily accessible for investigation and, mainly for the hysteresis effects, attractive for potential applications such as data storage [7], information processing [8] or voltage-controlled oscillators [9].

The cascade of phase transitions as a function of temperature includes the transition from the normal metallic to the incommensurate CDW (IC-CDW) phase, the nearly-commensurate CDW (NC-CDW) phase and the commensurate CDW (C-CDW) phase occurring at around $T_{IC} = 554$ K, $T_{NC} = 355$ K and in the temperature range from $T_{C\downarrow} = 180$ K to $T_{C\uparrow} = 230$ K, respectively. Recent studies indicate the possibility of yet another phase transition in $1T$-TaS_2 at T_H=80 K, named the hidden CDW state [10–12]. This discovery led to a new boost in attention for $1T$-TaS_2.

Upon lowering the temperature to $T_{IC} = 554$ K, the normal metallic state structure, described by the space group $P\bar{3}m1$ (D^d_{3d}), [13] transforms into the IC-CDW state. As will be demonstrated here, the IC-CDW domains shrink upon further temperature reduction until they gradually disappear, giving place to the C-CDW ordered state. This region in the phase diagram between 554 K and roughly 200 K is characterized by the coexistence of the IC-CDW and C-CDW phases and is often refereed to as NC-CDW. At the transition temperature T_C IC-CDW domains completely vanish [14] and a new lattice symmetry is established. There is general consensus about the formation of "star-of-David" clusters with in-plane $\sqrt{13}a \times \sqrt{13}a$ lattice reconstruction, whereby twelve Ta atoms are grouped around the $13^{\rm th}$ Ta atom [15, 16]. In the absence of any external strain fields, this can be achieved in two equivalent ways (by either clockwise or counterclockwise rotations) thus yielding domains [17]. In spite of extensive investigations, both experimental and theoretical, it remains an open question whether the stacking of "star-of-David" clusters is triclinic, trigonal, hexagonal or a combination thereof [15, 16, 18–20]. The C-CDW phase is believed to be an insulator [3, 21–23] with a gap of around 100 meV [13]. Very recent theoretical studies based on density-functional theory (DFT) find an additional ordering pattern along the crystallographic c-axis. The related gap has a width of approximately 0.5 eV along k_z and becomes gapped at the Fermi energy $E_{\rm F}$ in the C-CDW phase [24, 25].

Nearly all of the previously reported results for optical phonons in $1T$-TaS_2 are based on Raman spectroscopy on the C-CDW phase and on temperature-dependent measurements in a narrow range around the NC-CDW to

* Present address: Los Alamos National Laboratory, Los Alamos, New Mexico 87545, USA

C-CDW phase transition [13, 15, 18–20]. In this article we present temperature-dependent polarization-resolved Raman measurements in the temperature range from 4 K to 370 K covering all three CDW regimes of $1T$-TaS_2. Our analysis of the C-CDW phase confirms the symmetry to be $P\bar{3}$, while the NC-CDW phase is confirmed as a mixed regime of commensurate and incommensurate domains. The Raman spectra of the IC-CDW phase mainly project the phonon density of states due to breaking of translation invariance and sizeable electron-phonon coupling. The growth of the CDW gap upon cooling, followed by the opening of the Mott gap is traced via the initial slope of the symmetry-resolved spectra. The size of 170-190 meV and the temperature dependence of the Mott gap are directly determined from high-energy Raman data.

II. EXPERIMENTAL AND NUMERICAL METHODS

The preparation of the studied $1T$-TaS_2 single crystals is described elsewhere [26–29]. Calibrated customized Raman scattering equipment was used to obtain the spectra. Temperature-dependent measurements were performed with sample attached to the cold finger of a He-flow cryostat. The sample was cooled down to the lowest temperature and then heated. In either case the rates were less than ± 1 K/min. All measurements were performed in high vacuum of approximately $5 \cdot 10^{-5}$ Pa.

The 575 nm laser line of a diode-pumped Coherent GENESIS MX-SLM solid state laser was used as an excitation source. Additional measurements with the 458 nm and 514 nm laser lines were performed with a Coherent Innova 304C Argon ion laser. The absorbed power was set at 4 mW. All spectra shown are corrected for the sensitivity of the instrument and the Bose factor, yielding the imaginary part of the Raman susceptibility $R\chi''$ where R is an experimental constant. An angle of incidence of $\Theta_i = 66.0 \pm 0.4°$ and atomically flat cleaved surfaces enable us to measure at energies as low as $5\,\mathrm{cm}^{-1}$ without a detectable contribution from the laser-line since the directly reflected light does not reach the spectrometer. The corresponding laser spot has an area of roughly $50 \times 100\,\mu\mathrm{m}^2$ which prevents us from observing the possible emergence of the domains [17, 30]. The inelastically scattered light is collected along the surface normal (crystallographic c-axis) with an objective lens having a numerical aperture of 0.25. In the experiments presented here, the linear polarizations of the incident and scattered light are denoted as $\mathbf{e}_\mathrm{i}$ and $\mathbf{e}_\mathrm{s}$, respectively. For $\mathbf{e}_\mathrm{i}$ horizontal to the plane of incidence there is no projection on the crystallographic c-axis. For the low numerical aperture of the collection optics $\mathbf{e}_\mathrm{s}$ is always perpendicular to the c-axis. Low energy data up to $550\,\mathrm{cm}^{-1}$ were acquired in steps of $\Delta\Omega = 1\,\mathrm{cm}^{-1}$ with a resolution of $\sigma \approx 3\,\mathrm{cm}^{-1}$. The symmetric phonon lines were modelled using Voigt profiles where the width of the Gaussian part is given by σ. For spectra up to higher energies the step width and resolution were set at $\Delta\Omega = 50\,\mathrm{cm}^{-1}$ and $\sigma \approx 20\,\mathrm{cm}^{-1}$, respectively. The Raman tensors for the D_{3d} point group are given in Table I. Accordingly, parallel linear polarizations project both A_{1g} and E_g symmetries, while crossed linear polarizations only project E_g. The pure A_{1g} response then can be extracted by subtraction.

TABLE I. Raman tensors for trigonal systems (point group D_{3d})

$$A_{1g} = \begin{pmatrix} a & 0 & 0 \\ 0 & a & 0 \\ 0 & 0 & b \end{pmatrix} \quad {}^1E_g = \begin{pmatrix} c & 0 & 0 \\ 0 & -c & d \\ 0 & d & 0 \end{pmatrix} \quad {}^2E_g = \begin{pmatrix} 0 & -c & -d \\ -c & 0 & 0 \\ -d & 0 & 0 \end{pmatrix}$$

We have performed DFT calculations as implemented in the ABINIT package [31]. We have used the Perdew-Burke-Ernzerhof (PBE) functional, an energy cutoff of 50 Ha for the planewave basis, and we have included spin-orbit coupling by means of fully relativistic Goedecker pseudopotentials [32, 33], where Ta-$5d^36s^2$ and S-$3s^23p^4$ states are treated as valence electrons. The crystal structure was relaxed so that forces on each atom were below 10 μeV/Å and the total stress on the unit cell below 1 bar, yielding lattice parameters $a = 3.44$ Å and $c = 6.83$ Å. Subsequently, the phonons and the electron-phonon coupling (EPC) were obtained from density functional perturbation theory (DFPT) calculations, also within ABINIT [34]. Here, we have used an $18 \times 18 \times 12$ **k**-point grid for the electron wave vectors and a $6 \times 6 \times 4$ **q**-point grid for the phonon wave vectors. For the electronic occupation we employed Fermi-Dirac smearing with broadening factor $\sigma_\mathrm{FD} = 0.01$ Ha, which is sufficiently high to avoid unstable phonon modes related to the CDW phases.

III. RESULTS AND DISCUSSION

A. Lattice dynamics of the charge-density wave regimes

Temperature-dependent symmetry-resolved Raman spectra of $1T$-TaS_2 are presented in Fig. 1. It is obvious that their evolution with temperature is divided into three distinct ranges (IC-CDW, NC-CDW and C-CDW) as indicated. The lattice dynamics for each of these ranges will be treated separately in the first part of the manuscript. In the second part we address the electron dynamics.

1. C-CDW phase

At the lowest temperatures $1T$-TaS_2 exists in the commensurate C-CDW phase. Here, the atoms form so called "Star-of-David" clusters. Different studies report either

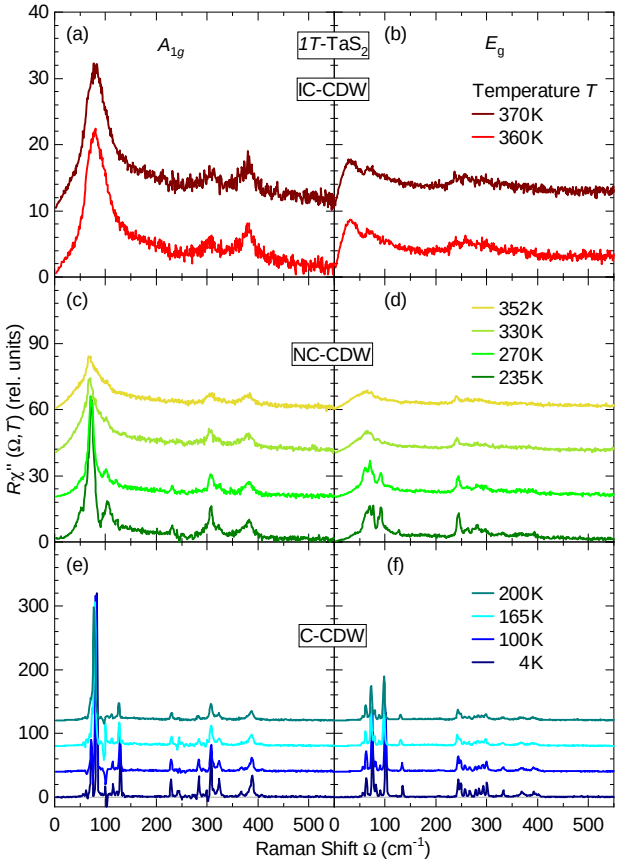

FIG. 1. Symmetry-resolved Raman spectra of $1T$-TaS_2 at temperatures as indicated. Both C-CDW (blue lines) and IC-CDW (red lines) domains yield significant contributions to the Raman spectra of the NC-CDW phase (green lines).

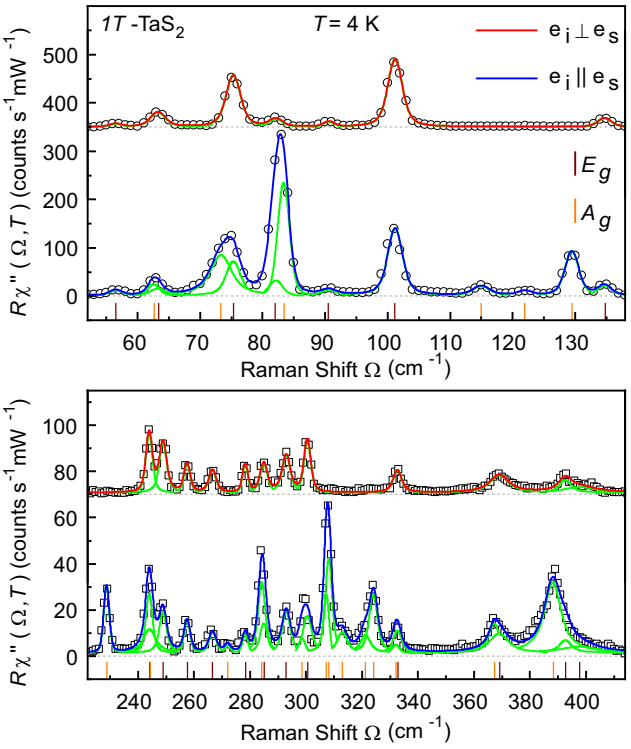

FIG. 2. Raman spectra at $T = 4\,\mathrm{K}$, i.e. in the C-CDW phase, for parallel and crossed light polarizations. Red and blue solid lines represent fits of the experimental data using Voigt profiles. Spectra are offset for clarity. The short vertical lines depict central frequencies obtained from the data analysis. The exact energy values are presented in Table II.

triclinic stacking of these clusters leading to $P\bar{1}$ unit cell symmetry [16], or trigonal or hexagonal stacking and $P\bar{3}$ unit cell symmetry [15, 18–20]. Factor group analysis predicts 57 A_g Raman-active modes with identical polarization-dependence for $P\bar{1}$ unit cell symmetry, and alternatively 19 A_g + 19 E_g Raman-active modes for $P\bar{3}$ unit cell symmetry [13] Our polarized Raman scattering measurements at $T = 4\,\mathrm{K}$, measured in two scattering channels, together with the corresponding cumulative fits are shown in Figure 2. As it can be seen, we have observed modes of two different symmetries in the related scattering channels. This result indicates trigonal or hexagonal stacking of the "Star-of-David" clusters. The symmetric phonon lines can be described by Voigt profiles, the best fit of which is shown as blue (for parallel light polarizations) and red (crossed polarizations) lines. After fitting Voigt profiles to the Raman spectra, 38 phonon modes were singled out. Following the selection rules for A_g and E_g symmetry modes, 19 were assigned as A_g and 19 as E_g symmetry, meaning all expected modes could be identified. The contribution from each mode to the cumulative fit is presented in Figure 2 as green lines, whereas the complete list of the corresponding phonon energies can be found in the Table II.

2. *IC-CDW phase*

At the highest experimentally accessible temperatures $1T$-TaS_2 adopts the IC-CDW phase. Data collected by Raman scattering at $T = 370\,\mathrm{K}$, containing all symmetries, is shown as a blue solid line in Figure 3. As $1T$-TaS_2 is metallic in this phase [35] we expect the phonon lines to be superimposed on a continuum of electron-hole excitations which we approximate using a Drude spectrum shown as a dashed line.[36, 37]

Since the IC-CDW phase arises from the normal metallic phase, described by space group $P\bar{3}m1$,[13, 38] it is interesting to compare our Raman results on the IC-CDW phase to an *ab initio* calculation of the phonon dispersion in the normal phase, shown as inset in Fig. 3. Four different optical modes were obtained at Γ: E_u at $189\,\mathrm{cm}^{-1}$ (double-degenerate), E_g at $247\,\mathrm{cm}^{-1}$ (double-degenerate), A_{2u} at $342\,\mathrm{cm}^{-1}$ and A_{1g} at $346\,\mathrm{cm}^{-1}$. Factor group analysis shows that two of these are Raman-active, namely E_g and A_{1g} [13].

We observe that the calculated phonon eigenvalues of the simple metallic phase at Γ do not closely match the

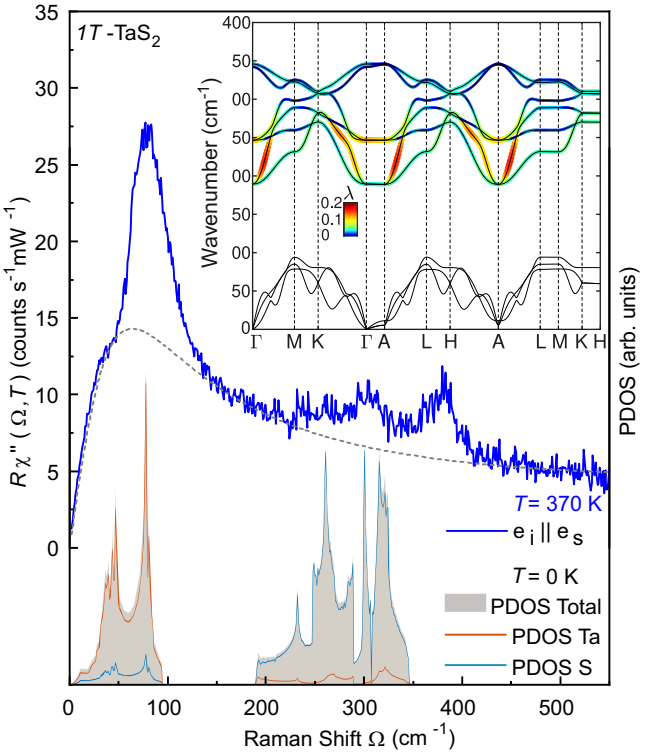

FIG. 3. Raman response for parallel light polarizations in the IC-CDW phase at 370 K (blue line). The dashed line depicts the possible electronic continuum. The contributions of the Ta- (dark brown) and S atoms (light brown) to the calculated PDOS (grey area) are shown below. The inset shows the calculated phonon dispersion of $1T$-TaS_2 in the simple metallic phase, with the electron-phonon coupling (λ) of the optical branches indicated through the color scale.

observed peaks in the experimental spectra of the IC-CDW phase. Rather, these correspond better to the calculated phonon density of states (PDOS), depicted in Fig. 3. There are essentially three different ways to project the PDOS in a Raman experiment and to overcome the $q \approx 0$ selection given by the small momentum of visible light: (i) Scattering on impurities [39], (ii) enhanced electron-phonon coupling [40], and (iii) breaking of the translational symmetry in the IC-CDW phase. (i) We rule out chemical impurity scattering, expected to exist at all temperatures, as the low-temperature spectra (Fig. 2) show no signs thereof. (ii) The additional scattering channel may come from the electron-phonon coupling (EPC). The calculated EPC, λ, in the optical modes (inset of Fig. 3) is limited, yet not negligible, reaching maxima of ~ 0.2 in the lower optical branches around Brillouin zone (BZ) points Γ and A. The calculated atom-resolved PDOS shows the acoustic modes to be predominantly due to Ta and the optical modes due to S, as a result of their difference in atomic mass. The acoustic modes display several dips that are signatures of the latent CDW phases, for which the EPC cannot be reliably determined. Significant EPC in the optical

TABLE II. A_{1g} and E_g Raman mode energies experimentally obtained at $T = 4$ K.

n_o	ω_{A_g}[cm^{-1}]	ω_{E_g}[cm^{-1}]
1	62.6	56.5
2	73.3	63.3
3	83.4	75.3
4	114.9	82.0
5	121.9	90.5
6	129.5	101.1
7	228.7	134.8
8	244.1	244.0
9	271.9	248.9
10	284.2	257.5
11	298.6	266.6
12	307.2	278.3
13	308.2	285.0
14	313.0	292.9
15	321.2	300.5
16	324.2	332.7
17	332.0	369.2
18	367.2	392.6
19	388.4	397.7

modes of $1T$-TaS_2 is furthermore supported by experimental results linking a sharp increase in the resistivity above the IC-CDW transition temperature to the EPC [38]. It also corroborates calculated [14] and experimentally obtained [13] values of the CDW gap, which correspond to intermediate to strong EPC [38]. (iii) Although EPC certainly contributes we believe that the majority of the additional scattering channels can be traced back to the incommensurate breaking of the translational invariance upon entering IC-CDW. Thus the "weighted" PDOS is projected into the Raman spectrum (see Fig. 1 (a) and (b)). These "weighting" factors depend on the specific symmetries along the phonon branches as well as the "new periodicity" and go well beyond the scope of this paper.

3. *NC-CDW phase*

The nearly-commensurate phase is seen as a mixed phase consisting of regions of commensurate and incommensurate CDWs [41, 42]. This coexistence of high and low-temperature phases is observable in our temperature dependent data as shown in Fig. 1. The spectra for the IC-CDW (red curves) and C-CDW phase (blue curves) are distinctly different, as also visible in the data shown above (Figs. 2 and 3). The spectra of the NC-CDW phase ($235\,\mathrm{K} < T < 352\,\mathrm{K}$) comprise contributions from both phases. As 352 K is the highest temperature at which the

contributions from the C-CDW phase can be observed in the spectra, we suggest that the phase transition temperature from IC-CDW to NC-CDW phase is somewhere in between 352 K and 360 K. This conclusion is in good agreement with experimental results regarding this transition [4–6].

B. Gap evolution

The opening of a typically momentum-dependent gap in the electronic excitation spectrum is a fundamental property of CDW systems which has also been observed in $1T$-TaS_2 [13, 38, 43]. Here, in addition to the CDW, a Mott transition at the onset of the C-CDW phase leads to an additional gap opening in the bands close to the Γ point [44, 45]. Symmetry-resolved Raman spectroscopy can provide additional information here using the momentum resolution provided by the selection rules. To this end, we look at the initial slopes of the electronic part of the spectra.

As shown in Fig. 4(a-c), different symmetries project individual parts of the BZ [37, 46]. The vertices given by the hexagonal symmetry of $1T$-TaS_2 are derived in Appendix C. The A_{1g} vertex mainly highlights the area around the Γ point while the E_g vertices predominantly project the BZ boundaries. The opening of a gap at the Fermi level reduces N_F, leading to an increase of the resistivity in the case of $1T$-TaS_2. This reduction of N_F manifests itself also in the Raman spectra which, to zeroth order, are proportional to N_F [36, 46]. As a result the initial slope changes as shown Figs. 4(d-e), which zooms in on the low energy region of the spectra from Fig. 1. The initial slope of the Raman response is $R \lim_{\Omega\to 0} \frac{\partial \chi''}{\partial \Omega} \propto N_F \tau_0$, where R incorporates only experimental factors [46]. The electronic relaxation $\Gamma_0^* \propto (N_F\tau_0)^{-1}$ is proportional to the dc resistivity $\rho(T)$ [47]. If a gap opens up there is vanishing intensity at $T = 0$ below the gap edge for an isotropic gap. At finite temperature there are thermally excited quasiparticle which scatter. Thus, there is a linear increase at low energies [36]. The black lines in Fig. 4(d-g) represent the initial slopes and their temperature dependences. The lines comprise carrier relaxation and gap effects, and we focus only on the relative changes.

Starting in the IC-CDW phase at $T = 370$ K [Fig. 4(d)] the initial slope is higher for the E_g spectrum than for A_{1g} symmetry. While the CDW gap started to open already at 554 K around the M points [44], which are highlighted by the E_g vertex, the Fermi surface projected by the E_g vertex continues to exist. Thus, we may interpret the different slopes as a manifestation of a momentum dependent gap in the IC-CDW phase and assume overall intensity effects to be symmetry-independent for all temperatures. At $T = 352$ K [Fig. 4(e)] the slope for E_g symmetry is substantially reduced to below the A_{1g} slope due to a strong increase of the CDW gap in the commensurate regions [44] which emerge upon entering the NC-CDW phase. Further cooling also decreases the slope for the A_{1g} spectrum, as the Mott gap around the Γ point starts to open within the continuously growing C-CDW domains[41, 42]. Below $T = 270$ K the initial slopes are identical for both symmetries and decrease with temperature. Apparently, the Mott gap opens up on the entire Fermi surface in direct correspondence with the increase of the resistivity by approximately an order of magnitude [3]. Finally, at the lowest temperature close to 4 K the initial slopes drop to almost zero [Fig. 4(g)] indicating vanishing conductivity or fully-gapped bands in the entire BZ.

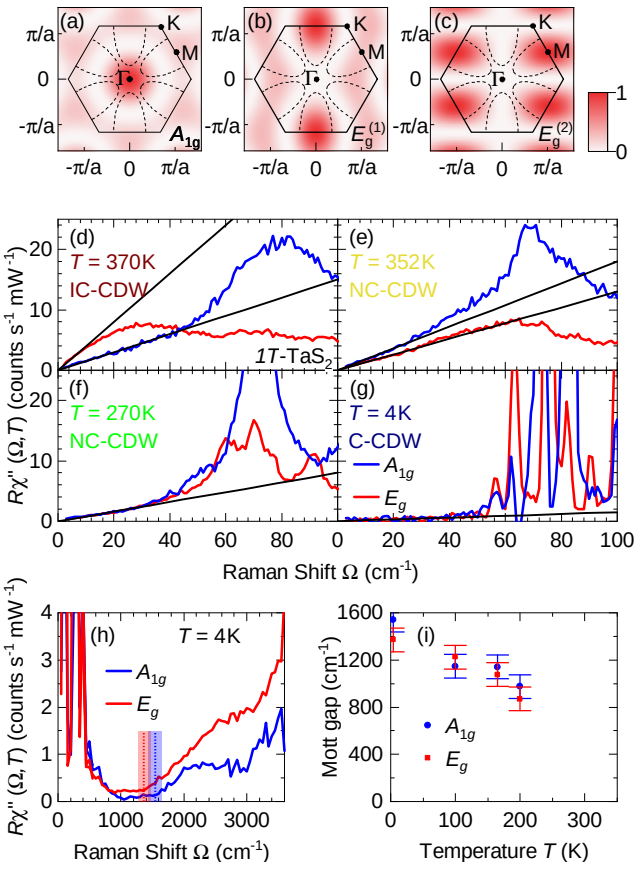

FIG. 4. Evolution of the gaps. (a-c) Squared Raman vertices and Fermi surface of $1T$-TaS_2 for the indicated symmetries in the normal phase above T_{IC}. The derivation of Raman vertices is presented in Appendix C. (d-g) Low energy Raman spectra for A_{1g} symmetry (blue) and E_g symmetries (red) at temperatures as indicated. The spectra shown are zooms on the data shown in Fig. 1. The black lines highlight the initial slope of the spectra. (h) High energy spectra at 4 K. Vertical dashed lines and colored bars indicate the approximate size and error bar of the Mott gap for the correspondingly colored spectrum. (i) Temperature dependence of the Mott gap Δ_μ ($\mu = A_{1g}, E_g$)

Concomitantly, and actually more intuitive for the opening of a gap, we observe the loss of intensity in the Raman spectra below a threshold at an energy Ω_{gap}. Below 30 cm^{-1} the intensity is smaller than

0.2 counts(mW s)$^{-1}$ [Fig. 4(g)] and still smaller than 0.3 counts(mW s)$^{-1}$ up to 1500 cm^{-1} [Fig. 4(h)]. For a superconductor or a CDW system the threshold is given by 2Δ, where Δ is the single-particle gap, and a pile-up of intensity for higher energies, $\Omega > 2\Delta$ [46]. A pile-up of intensity cannot be observed here. Rather, the overall intensity is further reduced with decreasing temperature as shown in the Appendix in Figs. 5 and 6. In particular, the reduction occurs in distinct steps between the phases and continuous inside the phases with strongest effect in the C-CDW phase below approximately 210 K [Fig. 5]. In a system as clean as 1T-TaS_2 the missing pile-up in the C-CDW phase is surprising and argues for an alternative interpretation.

In a Mott system, the gap persists to be observable but the pile-up is not a coherence phenomenon and has not been observed yet. In fact, the physics is quite different, and the conduction band is split symmetrically about the Fermi energy E_F into a lower and a upper Hubbard band. Thus in the case of Mott-Hubbard physics the experimental signatures are more like those expected for an insulator or semiconductor having a small gap, where at $T = 0$ there is a range without intensity and an interband onset with a band-dependent shape. At finite temperature there are thermal excitations inside the gap. For 1T-TaS_2 at the lowest accessible temperature, both symmetries exhibit a flat, nearly vanishing electronic continuum below a slightly symmetry-dependent threshold (superposed by the phonon lines at low energies). Above the threshold a weakly structured increase is observed. We interpret this onset as the distance of the lower Hubbard band from the Fermi energy E_F or half of the distance between the lower and the upper Hubbard band, shown as vertical dashed lines at 1350−1550 cm^{-1} ≡ 170−190 meV [Fig. 4(h)]. The energy is in good agreement with gap obtained from the in-plane ARPES[44], scanning tunneling spectroscopy [48] and infrared spectroscopy[13] which may be compared directly with our Raman results measured with in-plane polarizations. Upon increasing the temperature the size of the gap shrinks uniformly in both symmetries [Fig. 4(i)] and may point to an onset above the C-CDW phase transition, consistent with the result indicated by the initial slope. However, we cannot track the development of the gap into the NC-CDW phase as an increasing contribution of luminescence (see Appendix B) overlaps with the Raman data.

Recently, it was proposed on the basis of DFT calculations that 1T-TaS_2 orders also along the c-axis perpendicular to the planes in the C-CDW state [24, 35]. This quasi-1D coupling is unexpectedly strong and the resulting metallic band is predicted to have a width of approximately 0.5 eV. For specific relative ordering of the "star of David" patterns along the c-axis this band develops a gap of 0.15 eV at E_F[25] which is intriguingly close to the various experimental observations. However, since our light polarizations are strictly in-plane, we have to conclude that the gap observed here (and presumably in the other experiments) is an in-plane gap. Our experiment can not detect out-of-plane gap. Thus, neither a quasi-metallic dispersion along the c-axis nor a gap in this band along k_z may be excluded in the C-CDW phase. However, there is compelling evidence for a Mott-like gap in the layers rather than a CDW gap.

IV. CONCLUSIONS

We have presented a study of the various charge-density-wave regimes in 1T-TaS_2 by inelastic light scattering, supported by *ab initio* calculations. The spectra of lattice excitations in the commensurate CDW (C-CDW) phase determine the unit cell symmetry to be $P\bar{3}$, indicating trigonal or hexagonal stacking of the "star-of-David" structure. The high-temperature spectra of the incommensurate CDW (IC-CDW) state are dominated by a projection of the phonon density of states caused by either a significant electron-phonon coupling or, more likely, the superstructure. The intermediate nearly-commensurate (NC-CDW) phase is confirmed to be a mixed regime of commensurate and incommensurate regions contributing to the phonon spectra below an onset temperature $T_{NC} \approx 352 - 360$ K, in good agreement with previously reported values. At the lowest measured temperatures, the observation of a virtually clean gap without a redistribution of spectral weight from low to high energies below T_C argues for the existence of a Mott metal-insulator transition at a temperature of order 100 K. The magnitude of the gap is found to be $\Omega_{gap} \approx 170 - 190$ meV and has little symmetry, thus momentum, dependence in agreement with earlier ARPES results [38]. At 200 K, on the high-temperature end of the C-CDW phase, the gap shrinks to $\sim 60\%$ of its low-temperature value. Additionally, the progressive filling of the CDW gaps by thermal excitations is tracked via the initial slope of the spectra, and indicates that the Mott gap opens primarily on the parts of the Fermi surface closest to the Γ point.

Our results demonstrate the potential of using inelastic light scattering to probe the momentum-dependence and energy-scale of changes in the electronic structure driven by low-temperature collective quantum phenomena. This opens perspectives to investigate the effect of hybridization on collective quantum phenomena in heterostructures composed of different 2D materials, e.g., alternating T and H monolayers as in the *4Hb*-TaS_2 phase.[49]

ACKNOWLEDGEMENTS

The authors acknowledge funding provided by the Institute of Physics Belgrade through the grant by the Ministry of Education, Science and Technological Development of the Republic of Serbia. The work was supported by the Science Fund of the Republic of Serbia, PROMIS, No. 6062656, StrainedFeSC, and by Research

Foundation-Flanders (FWO). J.B. acknowledges support of a postdoctoral fellowship of the FWO, and of the Erasmus+ program for staff mobility and training (KA107, 2018) for a research stay at the Institute of Physics Belgrade, during which part of the work was carried out. The computational resources and services used for the first-principles calculations in this work were provided by the VSC (Flemish Supercomputer Center), funded by the FWO and the Flemish Government – department EWI. Work at Brookhaven is supported by the U.S. DOE under Contract No. DESC0012704. A. B. and R. H. acknowledge support by the German research foundation (DFG) via projects Ha2071/12-1 and 107745057 – TRR 80 and by the DAAD via the project-related personal exchange program PPP with Serbia grant-no. 57449106.

[1] J. C. Tsang, J. E. Smith, M. W. Shafer, and S. F. Meyer, Raman spectroscopy of the charge-density-wave state in $1T$- and $2H-TaSe_2$, Phys. Rev. B **16**, 4239 (1977).

[2] C. J. Sayers, H. Hedayat, A. Ceraso, F. Museur, M. Cattelan, L. S. Hart, L. S. Farrar, S. Dal Conte, G. Cerullo, C. Dallera, E. Da Como, and E. Carpene, Coherent phonons and the interplay between charge density wave and Mott phases in $1T-TaSe_2$, Phys. Rev. B **102**, 161105 (2020).

[3] A. J. Wilson, J. F. D. Salvo, and S. Mahajan, Charge-density waves and superlattices in the metallic layered transition metal dichalcogenides, Adv. Phys. **24**, 117 (1975).

[4] C. B. Scruby, P. M. Williams, and G. S. Parry, The role of charge density waves in structural transformations of $1T-TaS_2$, Philosophical Magazine **31**, 255 (1975).

[5] E. R. Thomson, B. Burk, A. Zettl, and J. Clarke, Scanning tunneling microscopy of the charge-density-wave structure in $1T-TaS_2$, Phys. Rev. B **49**, 16899 (1994).

[6] W. Wen, C. Dang, and L. Xie, Photoinduced phase transitions in two-dimensional charge-density-wave $1T-TaS_2$, Chin. Phys. B **28**, 058504 (2019).

[7] D. Svetin, I. Vaskivskyi, S. Brazovskii, Mertelj, and D. Mihailovic, Three-dimensional resistivity and switching between correlated electronic states in $1T-TaS_2$, Scientific Reports **7**, 46048 (2017).

[8] D. Svetin, I. Vaskivskyi, P. Sutar, E. Goreshnik, J. Gospodaric, T. Mertelj, and D. Mihailovic, Transitions between photoinduced macroscopic quantum states in $1T-TaS_2$ controlled by substrate strain, Applied Physics Express **7**, 103201 (2014).

[9] G. Liu, B. Debnath, T. R. Pope, T. T. Salguero, R. K. Lake, and A. A. Balandin, A charge-density wave oscillator based on an ntegrated tantalum disulfide-boron nitirde-graphene device operating at room temperature, Nature Nanotechnology **11**, 845 (2016).

[10] R. Salgado, A. Mohammadzadeh, F. Kargar, A. Geremew, C.-Y. Huang, M. A. Bloodgood, S. Rumyantsev, T. T. Salguero, and A. A. Balandin, Low-frequency noise spectroscopy of charge-density-wave phase transitions in vertical quasi-2d $1T-TaS_2$ devices, Applied Physics Express **12**, 037001 (2019).

[11] Z. X. Wang, Q. M. Liu, L. Y. Shi, S. J. Zhang, T. Lin, T. Dong, D. Wu, and N. L. Wang, Photoinduced hidden cdw state and relaxation dynamics of $1T-TaS_2$ probed by time-resolved terahertz spectroscopy, ArXiv e-prints (2019), arXiv:1906.01500.

[12] L. Stojchevska, I. Vaskivskyi, T. Mertelj, P. Kusar, D. Svetin, S. Brazovskii, and D. Mihailovic, Ultrafast switching to a stable hidden quantum state in an electronic crystal, Science **344**, 177 (2014).

[13] L. V. Gasparov, K. G. Brown, A. C. Wint, D. B. Tanner, H. Berger, G. Margaritondo, R. Gaál, and L. Forró, Phonon anomaly at the charge ordering transition in $1t-tas_2$, Phys. Rev. B **66**, 094301 (2002).

[14] O. R. Albertini, R. Zhao, R. L. McCann, S. Feng, M. Terrones, J. K. Freericks, J. A. Robinson, and A. Y. Liu, Zone-center phonons of bulk, few-layer, and monolayer $1T-TaS_2$: Detection of commensurate charge density wave phase through raman scattering, Phys. Rev. B **93**, 214109 (2016).

[15] S. Uchida and S. Sugai, Infrared and raman studies on a commensurate cdw states in transition metal dichalcogenides, Physica B+C **105B**, 393 (1981).

[16] R. Brouwer and F. Jellinek, The low-temperature superstructures of $1T-TaSe_2$ and $2H-TaSe_2$, Physica B+C **99**, 51 (1980).

[17] A. Zong, X. Shen, A. Kogar, L. Ye, C. Marks, D. Chowdhury, T. Rohwer, B. Freelon, S. Weathersby, R. Li, J. Yang, J. Checkelsky, X. Wang, and N. Gedik, Ultrafast manipulation of mirror domain walls in a charge density wave, Science Advances **4**, 10.1126/sciadv.aau5501 (2018).

[18] J. R. Duffay and R. D. Kirby, Raman scattering from $1T-TaS_2$, Solid State Communications **20**, 617 (1976).

[19] T. Hirata and F. S. Ohuchi, Temperature dependence of the raman spectra of $1T-TaS_2$, Solid State Communications **117**, 361 (2001).

[20] S. L. L. M. Ramos, R. Plumadore, S. W. H. J. Boddison-Chouinard, J. R. Guest, D. J. Gosztola, M. A. Pimenta, and A. Luican-Mayer, Suppression of the commensurate charge density wave phase in ultrathin $1T-TaS_2$ evidenced by raman hyperspectral analysis, Phys. Rev. B **100**, 165414 (2019).

[21] B. Sipos, A. F. Kusmartseva, A. Akrap, H. Berger, L. Forró, and E. Tutis, From mott state to superconductivity in $1T-TaS_2$, Nat. Mater. **12**, 960 (2008).

[22] P. Fazekas and E. Tosatti, Electrical, structural and magnetic properties of pure and doped $1T-TaS_2$, Philosophical Magazine Part B **39**, 229 (1979).

[23] E. Martino, A. Pisoni, L. Ćirić, A. Arakcheeva, H. Berger, A. Akrap, C. Putzke, P. J. W. Moll, I. Batistić, E. Tutiš, L. Forró, and K., Preferential out-of-plane conduction and quasi-one-dimensional electronic states in layered $1T-TaS_2$, npj 2D Mater Appl **4**, 7 (2020).

[24] P. Darancet, A. J. Millis, and C. A. Marianetti, Three-dimensional metallic and two-dimensional insulating behavior in octahedral tantalum dichalcogenides, Phys. Rev. B **90**, 045134 (2014).

[25] S.-H. Lee, J. S. Goh, and D. Cho, Origin of the Insulating Phase and First-Order Metal-Insulator Transition in $1T-TaS_2$, Phys. Rev. Lett. **122**, 106404 (2019).

[26] Y. Ma, Y. Hou, C. Lu, L. Li, and C. Petrovic, Possible origin of nonlinear conductivity and large dielectric constant in the commensurate charge-density-wave phase of 1T − TaS_2, Phys. Rev. B **97**, 195117 (2018).

[27] L. J. Li, W. J. Lu, X. D. Zhu, L. S. Ling, Z. Qu, and Y. P. Sun, Fe-doping induced superconductivity in the charge-density-wave system 1T − TaS_2, EPL (Europhysics Letters) **98**, 29902 (2012).

[28] Y. Liu, R. Ang, W. J. Lu, W. H. Song, L. J. Li, and Y. P. Sun, Superconductivity induced by se-doping in layered charge-density-wave system 1T − $TaS_{2-x}Se_x$, Applied Physics Letters **102**, 192602 (2013).

[29] R. Ang, Y. Miyata, E. Ieki, K. Nakayama, T. Sato, Y. Liu, W. J. Lu, Y. P. Sun, and T. Takahashi, Superconductivity and bandwidth-controlled mott metal-insulator transition in 1T − $TaS_{2-x}Se_x$, Phys. Rev. B **88**, 115145 (2013).

[30] M. Bovet, D. Popović, F. Clerc, C. Koitzsch, U. Probst, E. Bucher, H. Berger, D. Naumović, and P. Aebi, Pseudogapped Fermi surfaces of $1T - TaS_2$ and $1T - TaSe_2$: A charge density wave effect, Phys. Rev. B **69**, 125117 (2004).

[31] X. Gonze, B. Amadon, P.-M. Anglade, J.-M. Beuken, F. Bottin, P. Boulanger, F. Bruneval, D. Caliste, R. Caracas, M. Côté, T. Deutsch, L. Genovese, P. Ghosez, M. Giantomassi, S. Goedecker, D. Hamann, P. Hermet, F. Jollet, G. Jomard, S. Leroux, M. Mancini, S. Mazevet, M. Oliveira, G. Onida, Y. Pouillon, T. Rangel, G.-M. Rignanese, D. Sangalli, R. Shaltaf, M. Torrent, M. Verstraete, G. Zerah, and J. Zwanziger, Abinit: First-principles approach to material and nanosystem properties, Comput. Phys. Commun. **180**, 2582 (2009).

[32] S. Goedecker, M. Teter, and J. Hutter, Separable dual-space Gaussian pseudopotentials, Phys. Rev. B **54**, 1703 (1996).

[33] M. Krack, Pseudopotentials for H to Kr optimized for gradient-corrected exchange-correlation functionals, Theor. Chem. Acc. **114**, 145 (2005).

[34] X. Gonze, D. C. Allan, and M. P. Teter, Dielectric tensor, effective charges, and phonons in α-quartz by variational density-functional perturbation theory, Phys. Rev. Lett. **68**, 3603 (1992).

[35] S.-H. Lee, J. S. Goh, and D. Cho, Origin of the insulating phase and first-order metal-insulator transition in 1T − TaS_2, Phys. Rev. Lett. **122**, 106404 (2019).

[36] A. Zawadowski and M. Cardona, Theory of Raman scattering on normal metals with impurities, Phys. Rev. B **42**, 10732 (1990).

[37] N. Lazarević and R. Hackl, Fluctuations and pairing in fe-based superconductors: light scattering experiments, Journal of Physics: Condensed Matter **32**, 413001 (2020).

[38] K. Rossnagel, On the origin of charge-density waves in select layered transition-metal dichalcogenides, Journal of Physics: Condensed Matter **23**, 213001 (2011).

[39] R. Shuker and R. W. Gammon, Raman-scattering selection-rule breaking and the density of states in amorphous materials, Phys. Rev. Lett. **25**, 222 (1970).

[40] A. Baum, A. Milosavljević, N. Lazarević, M. M. Radonjić, B. Nikolić, M. Mitschek, Z. I. Maranloo, M. Šćepanović, M. Grujić-Brojčin, N. Stojilović, M. Opel, A. Wang, C. Petrovic, Z. V. Popović, and R. Hackl, Phonon anomalies in fes, Phys. Rev. B **97**, 054306 (2018).

[41] A. Spijkerman, J. L. de Boer, A. Meetsma, G. A. Wiegers, and S. van Smaalen, X-ray crystal-structure refinement of the nearly commensurate phase of 1T − TaS_2 in (3+2)-dimensional superspace, Phys. Rev. B **56**, 13757 (1997).

[42] R. He, J. Okamoto, Z. Ye, G. Ye, H. Anderson, X. Dai, X. Wu, J. Hu, Y. Liu, W. Lu, Y. Sun, A. N. Pasupathy, and A. W. Tsen, Distinct surface and bulk charge density waves in ultrathin 1T − TaS_2, Phys. Rev. B **94**, 201108 (2016).

[43] G. Grüner, The dynamics of charge-density waves, Rev. Mod. Phys. **60**, 1129 (1988).

[44] C. Sohrt, A. Stange, M. Bauer, and K. Rossnagel, How fast can a peierls–mott insulator be melted?, Faraday Discuss. **171**, 243 (2014).

[45] B. Sipos, A. F. Kusmartseva, A. Akrap, H. Berger, L. Forró, and E. Tutiš, From mott state to superconductivity in 1T − TaS_2, Nature Materials **7**, 960–965 (2008).

[46] T. P. Devereaux and R. Hackl, Inelastic light scattering from correlated electrons, Rev. Mod. Phys. **79**, 175 (2007).

[47] M. Opel, R. Nemetschek, C. Hoffmann, R. Philipp, P. F. Müller, R. Hackl, I. Tüttő, A. Erb, B. Revaz, E. Walker, H. Berger, and L. Forró, Carrier relaxation, pseudogap, and superconducting gap in high-T_c cuprates: A Raman scattering study, Phys. Rev. B **61**, 9752 (2000).

[48] J. Skolimowski, Y. Gerasimenko, and R. Žitko, Mottness collapse without metallization in the domain wall of the triangular-lattice Mott insulator $1T - TaS_2$, Phys. Rev. Lett. **122**, 036802 (2019).

[49] A. Ribak, R. M. Skiff, M. Mograbi, P. K. Rout, M. H. Fischer, J. Ruhman, K. Chashka, Y. Dagan, and A. Kanigel, Chiral superconductivity in the alternate stacking compound 4Hb-TaS_2, Science Advances **6**, eaax9480 (2020).

[50] P. B. Allen, Fermi-surface harmonics - general method for nonspherical problems - application to boltzmann and eliashberg equations, Phys. Rev. B **13**, 1416 (1976).

[51] M. S. Dresselhaus, G. Dresselhaus, and A. Jorio, *Group Theory* (Springer, 2008).

Appendix A: Raw data

Figure 5 shows Raman spectra at temperatures ranging from $T = 4\,\mathrm{K}$ to $370\,\mathrm{K}$ for parallel [panel (a)] and crossed [panel (b)] in-plane light polarizations. The spectra were measured in steps of $\Delta\Omega = 50\,\mathrm{cm}^{-1}$ and a resolution of $\sigma \approx 20\,\mathrm{cm}^{-1}$. Therefore neither the shapes nor the positions of the phonon lines below $500\,\mathrm{cm}^{-1}$ may be resolved. All spectra reach a minimum in the range from 500 to 1600 wn. At energies above $500\,\mathrm{cm}^{-1}$ the overall intensities are strongly temperature dependent and decreasing with decreasing temperature. Three clusters of spectra are well separated according to the phases they belong to.

In the C-CDW phase ($T \leq 200\,K$, blue lines) the spectra start to develop substructures at 1500 and $3000\,\mathrm{cm}^{-1}$. The spectra at 200 K increase almost linearly with energy. The spectra of the NC- and IC-CDW phases exhibit a broad maximum centered in the region of 2200-$3200\,\mathrm{cm}^{-1}$ which may be attributed to luminescence (see Appendix B). For clarification we measured a few spectra with various laser lines for excitation.

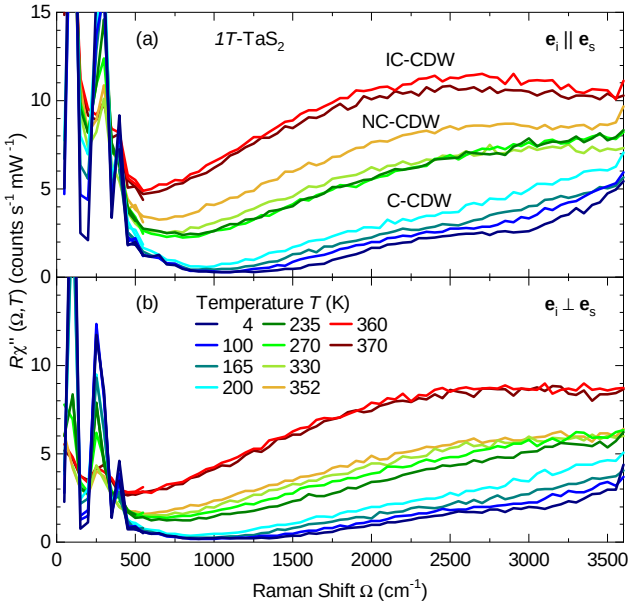

FIG. 5. Raman spectra up to high energies for (a) parallel and (b) crossed polarizations of the incident and scattered light at temperatures as given in the legend.

Appendix B: Luminescence

Figure 6 shows Raman spectra measured with parallel light polarizations for three different wavelengths λ_i of the incident laser light. Panels (a-b) depict the measured intensity I (without the Bose factor) as a function of the absolute frequency $\tilde{\nu}$ of the scattered light.

At high temperature [$T = 330\,\mathrm{K}$, panel(a)] a broad peak can be seen for all λ_i which is centered at a fixed frequency of $15200\,\mathrm{cm}^{-1}$ of the scattered photons (grey shaded area). The peak intensity decreases for increasing λ_i (decreasing energy). Correspondingly, this peak's center depends on the laser wavelength in the spectra shown as a function of the Raman shift [panel (c)]. This behaviour indicates that the origin of this excitation is likely to be luminescence where transitions at fixed absolute final frequencies are expected.

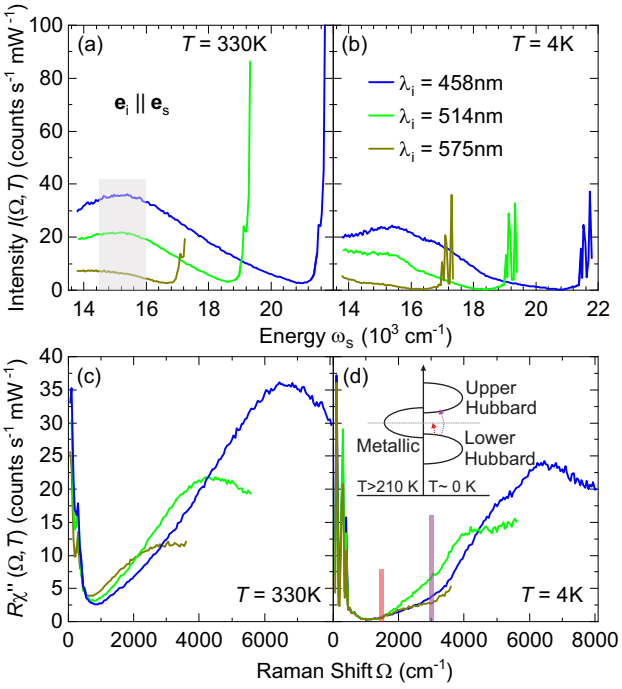

FIG. 6. Luminescence contribution to the Raman data. (a-b) Intensity as a function of the absolute frequency for (a) $T = 330\,\mathrm{K}$ and (b) $T = 4\,\mathrm{K}$. The approximate peak maximum of the contribution attributed to luminescence is highlighted by the gray shaded area. (c-d) Raman susceptibility calculated from panels (a) and (b), respectively, shown as a function of frequency (Raman) shift. The luminescence peak appears at different Raman shifts depending on the wavelength of the laser light. At $T = 4\,\mathrm{K}$ the spectra are identical up to $1600\,\mathrm{cm}^{-1}$ for all laser light wavelengths.

At low temperature [Fig. 6(b)] we cannot find a structure at a fixed absolute energy any further. Rather, as already indicated in the main part, the spectra develop additional, yet weak, structures which are observable in all spectra but are particularly pronounced for blue excitation. For green and yellow excitation the spectral range of the spectrometer, limited to 732 nm, is not wide enough for deeper insight into luminescence contributions (at energies different from those at high temperature) and no maximum common to all three spectra is observed. If these spectra are plotted as a function of the Raman shift the changes in slope at 1500 and $3000\,\mathrm{cm}^{-1}$ are found to be in the same position for all λ_i values thus arguing for inelastic scattering rather than luminescence. Since we do currently not have the appropriate experimental tools

for an in-depth study our interpretation is preliminary although supported by the observations in Fig. 6(d).

As shown in the inset of Fig. 6(d) we propose a scenario on the basis of Mott physics. In the C-CDW phase the reduced band width is not the largest energy any further and the Coulomb repulsion U becomes relevant [22] and splits the conduction band into a lower and upper Hubbard band. We assume that the onset of scattering at $1500\,\mathrm{cm}^{-1}$ corresponds to the distance of the highest energy of the lower Hubbard band to the Fermi energy E_F. The second onset corresponds then to the distance between the highest energy of the lower Hubbard band and the lowest energy of the upper Hubbard band. An important question needs to be answered: Into which unoccupied states right above E_F the first process scatters electrons. We may speculate that some DOS is provided by the metallic band dispersing along k_z or by the metallic domain walls between the different types of ordering patterns along the c-axis observed recently by tunneling spectroscopy [48]. These quasi-1D domain walls would provide the states required for the onset of scattering at high energy but are topologically too small for providing enough density of states for measurable intensity at low energy [Fig. 4(g)] in a location-integrated experiment like Raman scattering.

Appendix C: Derivation of the Raman vertices

Phenomenologically, the Raman vertex can be derived based on lattice symmetry, which are proportional to the Brillouin zone harmonics. They are a set of functions that exhibit the symmetry and periodicity of the lattice structure proposed by Allen [50]. These functions make the k-space sums and energy integrals more convenient than that of the Cartesian basis or the spherical harmonics basis, especially for those materials who have an-isotropic and/or multiple Fermi pockets. The three Cartesian components of the Fermi velocity v_k are recommended to generate this set of functions since they inherit the symmetry and periodicity of the crystal lattice naturally. However, in most cases, we do not know the details of band dispersion. A phenomenological method is needed to construct such a set of basis functions. Here, we demonstrate a method based on the group theory. The Brillouin zone harmonics can be obtained by the projection operation on specific trial functions.

For a certain group G with symmetry elements R and symmetry operators $\hat{P}_R$, it can be described by several irreducible representations Γ_n, where n labels the representation. For each irreducible representation, there are corresponding basis functions $\Phi^j_{\Gamma_n}$ that can be used to generate representation matrices for a particular symmetry. Here, j labels the component or partner of the representations. For an arbitrary function F, we have

$$F = \sum_{\Gamma_n}\sum_{j} f_j^{\Gamma_n}\Phi^j_{\Gamma_n}, \tag{C1}$$

TABLE III. Symmetry operations $\hat{P}_R$ and corresponding character table of D_{3d} point group

$\hat{P}_R$	x'	y'	z'	$\chi^{\Gamma_n}(R)$ A_{1g}	E_g
E	x	y	z	1	2
C_3^1	$-\frac{1}{2}x+\frac{\sqrt{3}}{2}y$	$-\frac{\sqrt{3}}{2}x-\frac{1}{2}y$	z	1	-1
C_3^{-1}	$-\frac{1}{2}x-\frac{\sqrt{3}}{2}y$	$\frac{\sqrt{3}}{2}x-\frac{1}{2}y$	z	1	-1
$C_2^{'}$	x	$-y$	$-z$	1	0
$C_2^{''}$	$-\frac{1}{2}x+\frac{\sqrt{3}}{2}y$	$\frac{\sqrt{3}}{2}x+\frac{1}{2}y$	$-z$	1	0
$C_2^{'''}$	$-\frac{1}{2}x-\frac{\sqrt{3}}{2}y$	$-\frac{\sqrt{3}}{2}x+\frac{1}{2}y$	$-z$	1	0
I	$-x$	$-y$	$-z$	1	2
S_6^1	$\frac{1}{2}x-\frac{\sqrt{3}}{2}y$	$\frac{\sqrt{3}}{2}x+\frac{1}{2}y$	$-z$	1	-1
S_6^{-1}	$\frac{1}{2}x+\frac{\sqrt{3}}{2}y$	$-\frac{\sqrt{3}}{2}x+\frac{1}{2}y$	$-z$	1	-1
$\sigma_v^{'}$	$-x$	y	z	1	0
$\sigma_v^{''}$	$\frac{1}{2}x-\frac{\sqrt{3}}{2}y$	$-\frac{\sqrt{3}}{2}x-\frac{1}{2}y$	z	1	0
$\sigma_v^{'''}$	$\frac{1}{2}x+\frac{\sqrt{3}}{2}y$	$\frac{\sqrt{3}}{2}x-\frac{1}{2}y$	z	1	0

According to the group theory, we can always define a projection operator by the relation [51]:

$$\hat{P}^{\Gamma_n} = \frac{d}{N}\sum_R \chi^{\Gamma_n}(R) * \hat{P}_R, \tag{C2}$$

that satisfies the relation:

$$\hat{P}^{\Gamma_n} F = \sum_j f_j^{\Gamma_n}\Phi^j_{\Gamma_n}, \tag{C3}$$

where d is the dimensionality of the irreducible representation Γ_n, N is the number of symmetry operators in the group and $\chi^{\Gamma_n}(R)$ is the character of the matrix of symmetry operator R in irreducible representation Γ_n. By projection operation on a certain irreducible representation Γ_n, we can directly get its basis functions $\Phi^j_{\Gamma_n}$.

The basis functions are not unique. In specific physical problems, it is useful to use physical insight to guess an appropriate arbitrary function to find the basis functions for specific problems. 1T-TaS_2 belongs to D_{3d} point group. There are 12 symmetry operators in this group, i.e. E, C_3^1, C_3^{-1}, $C_2^{'}$, $C_2^{''}$, $C_2^{'''}$, I, S_6^1, S_6^{-1}, $\sigma_v^{'}$, $\sigma_v^{''}$, $\sigma_v^{'''}$. The coordinates transformation after symmetry operations and the corresponding character table are listed in Tab. III.

In order to simulate the perodicity of the Brillouin zone, trigonometric functions are used as trial functions. According to the parity of the irreducible representations, we can choose appropriate trigonometric function, e.g. sine function for odd parity representation and cosine function for even parity representation. The combinations of them are also available.

Here, we use $F = \cos(\mathrm{k_x a})$ as a trial function, where a is the in-plane crystal constant. The basis function of A_{1g} can be derived as:

$$\Phi_{A_1g}(\mathbf{k}) = \frac{1}{3}\left[\cos(\mathrm{k_x a}) + 2\cos\left(\frac{1}{2}\mathrm{k_x a}\right)\cos\left(\frac{\sqrt{3}}{2}\mathrm{k_y a}\right)\right] \tag{C4}$$

With the same method, we obtain a basis functions of E_g as:

$$\Phi_{E_g^1}(\mathbf{k}) = \frac{2}{3}\left[\cos(\mathrm{k_x a}) - \cos\left(\frac{1}{2}\mathrm{k_x a}\right)\cos\left(\frac{\sqrt{3}}{2}\mathrm{k_y a}\right)\right]. \tag{C5}$$

Since the E_g is a two-dimensional representation, the projection operation provides only one of the two basis functions of the corresponding subspace. The second function is found based on the subspace invariance under the symmetry operations (e.g. if we operate $\Phi_{E_g^1}$ with C_3^1 symmetry, result can be presented as an linear combination of $\Phi_{E_g^1}$ and $\Phi_{E_g^2}$). Thus we obtain:

$$\Phi_{E_g^2}(\mathbf{k}) = 2\sin\left(\frac{1}{2}\mathrm{k_x a}\right)\sin\left(\frac{\sqrt{3}}{2}\mathrm{k_y a}\right). \tag{C6}$$